Journal of Volcanology and Geothermal Research 443 (2023) 107931

Contents lists available at ScienceDirect

Journal of Volcanology and Geothermal Research

journal homepage: www.journals.elsevier.com/journal-of-volcanology-and-geothermal-research

Magma and hydrothermal sources below the northern part of Paramushir Island (Kuril Arc) inferred from ambient noise tomography

Nadezhda Belovezhets [a,b,c], Yaroslav Berezhnev [a,b,c], Ivan Koulakov [a,c,d,*], Andrey Jakovlev [e], Sergei Abramenkov [b,c], Sergey Z. Smirnov [f], Ilyas Abkadyrov [g]

[a] *Skolkovo Institute of Science and Technology (Skoltech), Bolshoy Blrd 30/1, Moscow 121205, Russia*
[b] *Novosibirsk State University, Pirogova 2, 630090 Novosibirsk, Russia*
[c] *Trofimuk Institute of Petroleum Geology and Geophysics SB RAS, Prospekt Koptyuga, 3, 630090 Novosibirsk, Russia*
[d] *Institute of the Earth's Crust SB RAS, Irkutsk, Russia*
[e] *Alfred-Wegener-Institut, Am Alten Hafen 26, 27568 Bremerhaven, Germany*
[f] *Sobolev Institute of Geology and Mineralogy SB RAS, Prospekt Koptyuga, 3, 630090 Novosibirsk, Russia*
[g] *Institute of Volcanology and Seismology, FEB RAS, Petropavlovsk-Kamchatsky, Russian Federation*

ARTICLE INFO

Keywords:
Ebeko volcano
Kuril Islands
Ambient Noise
Surface wave
Seismic Tomography

ABSTRACT

Paramushir is the northernmost island of the Kuril Arc comprising several Holocene volcanoes, of which two are presently active: Ebeko and Chikurachki. We present the first crustal-scale three-dimensional seismic shear-wave velocity model of the northern part of Paramushir derived with the use of data of 20 temporary stations operated in 2021–2022 and one permanent station. The continuous seismic data were used to obtain the Rayleigh wave dispersion curves for periods ranging from 0.5 s to 12 s through computing ambient seismic noise cross-correlation functions. Then the 3D shear wave velocity distribution was constructed by seismic tomography. The synthetic tests demonstrate that the model has sufficient resolution down to 7–10 km depth. We observe a series of low-velocity anomalies at the depths of 4–6 km below the volcano-origin Vernadsky Ridge. They may likely represent magma reservoirs that are responsible for Holocene eruptions along the ridge. These anomalies are overlain by the high-velocity anomalies associated with the rigid cover consisting of an upper-crustal granite-granodiorite body and consolidated magma intrusions. Along the eastern flank of Ebeko we reveal a thin low-velocity anomaly at a depth of ~1 km that can be interpreted as a water-saturated layer. The contact of this layer with hot magma intrusions leads to the formation of a large amount of steam that is ejected during the frequent phreatic eruptions of Ebeko and from numerous fumaroles in the summit area. On the other hand, this layer, which is following down to the Pacific Coast, might be promising for the geothermal energy exploitation.

1. Introduction

Volcanic eruptions and related ash and gas ejections might represent serious hazards to the population, infrastructure and transportation in surrounding areas. Expanding our knowledge about processes inside magmatic and geothermal volcanic systems makes it possible to improve eruption forecast criteria and, therefore, minimize negative effects caused by the volcanic activity. Furthermore, volcanoes provide an unlimited green energy source, which can be used for the needs of the local population (e.g., Wohletz and Heiken, 1992; Duffield and Sass, 2003). These and other reasons require performing geophysical surveys giving the information about physical properties of the medium. Ambient seismic noise tomography is among the most powerful geophysical techniques providing high-quality models beneath volcanoes (e.g., Masterlark et al., 2010; Jaxybulatov et al., 2014; Bai et al., 2021; Mordret et al., 2015; Obermann et al., 2016). It is especially challenging to study volcanoes located in hard-to-reach areas of Kamchatka and the Kuril Islands. One of such sites is active Ebeko Volcano located on Paramushir Island in the Kuril Arc that is considered in this study. The volcanic activity in Kamchatka and Kuril Islands is mostly controlled by the ongoing subduction of the Pacific Plate.

The eruption activity of Ebeko poses serious problems to the population and infrastructure of Severo-Kurilsk, a town with ~3000 inhabitants located at only 6–7 km from the active vent of Ebeko. Due to a

* Corresponding author at: Skolkovo Institute of Science and Technology (Skoltech), Bolshoy Blrd 30/1, Moscow 121205, Russia.
E-mail address: ivan.science@gmail.com (I. Koulakov).

https://doi.org/10.1016/j.jvolgeores.2023.107931
Received 13 July 2023; Received in revised form 5 October 2023; Accepted 8 October 2023
Available online 14 October 2023

dominant wind direction from the west, the town suffers from the ash and gas ejected during the frequent eruptions. Probably the most harmful event which might threaten the town are lahars. For the last 4.5–5 thousand years five to six powerful lahars have descended along the Matrosskaya river valley (Laverov et al., 2005). Notably, most part of the modern Severo-Kurilsk town has been built upon a surface of such lahar, which occurred 5700 years ago (Melekestsev et al., 1993). A serious hazard related to the activity of Ebeko requires thorough monitoring and assessment of the possible catastrophic scenarios including ashfalls, gas incursions and lahars. The ash clouds from Ebeko ejecting during strong eruptions may also affect the air and maritime traffic, which is active in this segment of the Pacific Ocean. All these reasons determine the importance of conducting multidisciplinary studies of this volcano.

Another problem is that the electricity and heat for Severo-Kurilsk town is presently supplied by a diesel-based power plant, and delivering the fuel to the island is tooexpensive. This determines the importance of geothermal exploration to provide the cheap and green energy for the town needs. Based on the existing geophysical and geological information, the total geothermal energy potential of Paramushir Island is estimated at 60–100 MW for at least 100 years of exploitation (Belousov et al., 2002). These resources are mostly associated with the North-Paramushir hydrothermal-magmatic field around the presently active Ebeko Volcano. On the other hand, Belousov et al. (2021) claim that the hydrothermal system around Ebeko is superficial and has a small volume, therefore, it is not suitable for geothermal energy exploitation. To shed light on this, reliable and sufficiently detailed geophysical models of the deep structures below Paramushir Island are required.

A number of multiscale and multidisciplinary geophysical surveys have provided the information on structures beneath Paramushir and surrounding areas at different depths. The shape of the slab was inferred from the regional and global scale seismic tomography studies based on the data from the international and regional catalogs (e.g., Gorbatov et al., 2001; Jiang et al., 2009; Koulakov et al., 2011). The data of the slab-related seismicity recorded by regional seismic networks of GS RAS were used by Bergal-Kuvikas et al. (2023) to study the upper mantle and crustal structures in the junction area of Kamchatka and the Kuril Islands including Paramushir. However, the resolution of this model was too low to derive any information about the magmatic and hydrothermal processes below Ebeko.

Note that the only one permanent seismic station SKR operated by Geophysical Survey of Russian Academy of Sciences (GS RAS) is located on Paramushir. The other nearest seismic stations are located at large distances: one on the Atlasov Island (45 km) and a few others in southern Kamchatka (>100 km). All together, they can be used to localize strong earthquakes, but are not suitable to study the volcano-related seismicity and structures beneath Ebeko Volcano.

Regional-scale deep seismic sounding was performed in 1957–1958 in areas around Paramushir (Zlobin, 1987). The crustal thickness below Paramushir Island is estimated as 22–24 km based on the seismic data (*Atlas of Geology and Geophysics in the Kuril-Kamchatka Arc System,* 1987). Airborne gravity and magnetic surveys of the northern Kuril Islands were conducted in the 1960s and in 1991 (Shustova, 1992). A prominent negative gravity anomaly was identified below the central cone of Ebeko, which was interpreted as a low-density conduit body.

Local-scale geophysical surveys on Paramushir Island started from the late 1950s. However, most of the results were not published in open sources and can only be found in archived technical reports. Electrical surveys aimed at finding water sources for Severo-Kurilsk were performed within several campaigns from 1960s to 1990s using vertical electrical sounding (VES) reaching depths of up to 500 m (Bogdanov, 1981). Frequency-domain electromagnetic sounding and some sparse magnetotelluric measurements were carried out in 1992 (Shmeleva, 1993) and then reprocessed by Kiryukhin (2000). Most of these electrical surveys were conducted near the Pacific coast of Paramushir Island and only reached depths of a few hundred meters. The areas of Vernadsky Ridge and the western flank of the island were never explored with any geophysical surveys, except for airborne magnetic and gravity measurements (Shustova, 1992). Therefore, no geophysical information on the mid-deep structures at depths of >1 km have been previously obtained on Paramushir yet.

In 1994, several boreholes were drilled in the vicinity of the city of Severo-Kurilsk. Only one of three deep wells with depths of >1 km has provided some moderate hot water outcome. The deepest well GP3 reached the depth of 2500 m, but did not reveal any water sources (Belousov et al., 2002; Rychagov et al., 2002). The maximum measured temperature of dry rocks in these wells was 210 °C. No boreholes on Vernadsky Ridge or on its western flanks were ever drilled.

After a generally unsuccessful outcome of the geophysical campaigns and drilling, any attempts to explore the geothermal resources on Paramushir have been stopped for more than twenty years. At the same time, the fact of very high fumarolic and eruption activity of Ebeko indicates that it is promising for energy production for the town's needs. That is why it is important to continue studying the magmatic and hydrothermal system structure beneath Ebeko volcano using novel technologies such as ambient noise tomography. In this study, owing to the deployment of a seismic network on Paramushir Island, we have obtained the first 3D shear-wave seismic velocity model, which unambiguously infers the location of the magma reservoir and indicates possible hydrothermal structures.

2. Geological settings

Paramushir Island is the second largest island of the Kuril Arc with an area of approximately 2000 km^2, with the length of 100 km and the width of 20–25 km. It is located in the northern part of the Kuril Arc on the southern end of continental shelf of Kamchatka peninsula (Markhanov and Potapyev, 1981; Bergal-Kuvikas et al., 2023) (Fig. 1A) and it separates the Sea of Okhotsk from the northwestern Pacific Ocean. The tectonic and volcanic activity of Paramushir is controlled by the ongoing subduction of the Pacific Plate having almost orthogonal direction and a rate of 7.8 cm/year (Avdeiko et al., 2007).

Paramushir Island is built up of two major rock complexes (State Geological Map, 2001). The lower one is the Upper Miocene to Pliocene basement composed of volcanogenic sedimentary and sedimentary rocks dissected by major faults and broken by Tertiary intrusive massifs and subvolcanic bodies (sills and dikes). One of such bodies is a large exhumed sill composing the perfectly flat Aerodrom Plateau, which during the Second World War was used by the Japanese as an air-force base. The basement is overlayed by a Quaternary sequence of thick volcanic formations with the age of Early Pleistocene to Holocene, and minor glacial, alluvial and other unconsolidated Mid-Pleistocene to Holocene deposits (Gorshkov, 1970; Fedorchenko et al., 1989; State Geological Map, 2001).

Paramushir Island is divided by two major fault zones into three terraines - Northern, Middle and Southern. The Northern and Southern parts corresponding to the Vernadsky and Karpinsky ridges are active volcanic terrains, while the Middle one is presently volcanically inactive. On Paramushir Island, there are at least 11 volcanoes that have been active in the Holocene. Ebeko group and several more volcanoes are located in the northern terrain; Chikurachki, Lomonosov, Tatarinov, Fuss Peak, and Karpinsky group are in the southern terrain. Two of them, Ebeko and Chikurachki, presently show eruption activity. Several ridges of volcanic nature (Vernadsky, Levinson-Lessing and Karpinsky) constitute the major topographic features of Paramushir Island.

In this study, we mostly focus on the northern part of Paramushir, in which the major topographic feature is the north-south oriented Vernadsky Ridge having a length of ~25 km and an altitude of around 1000 m (Fig. 1B). Volcanic activity in this area started in the Early Pleistocene with massive eruptions of lava flows from the vents located in the vicinity of the ridge crest. This led to almost complete transformation of

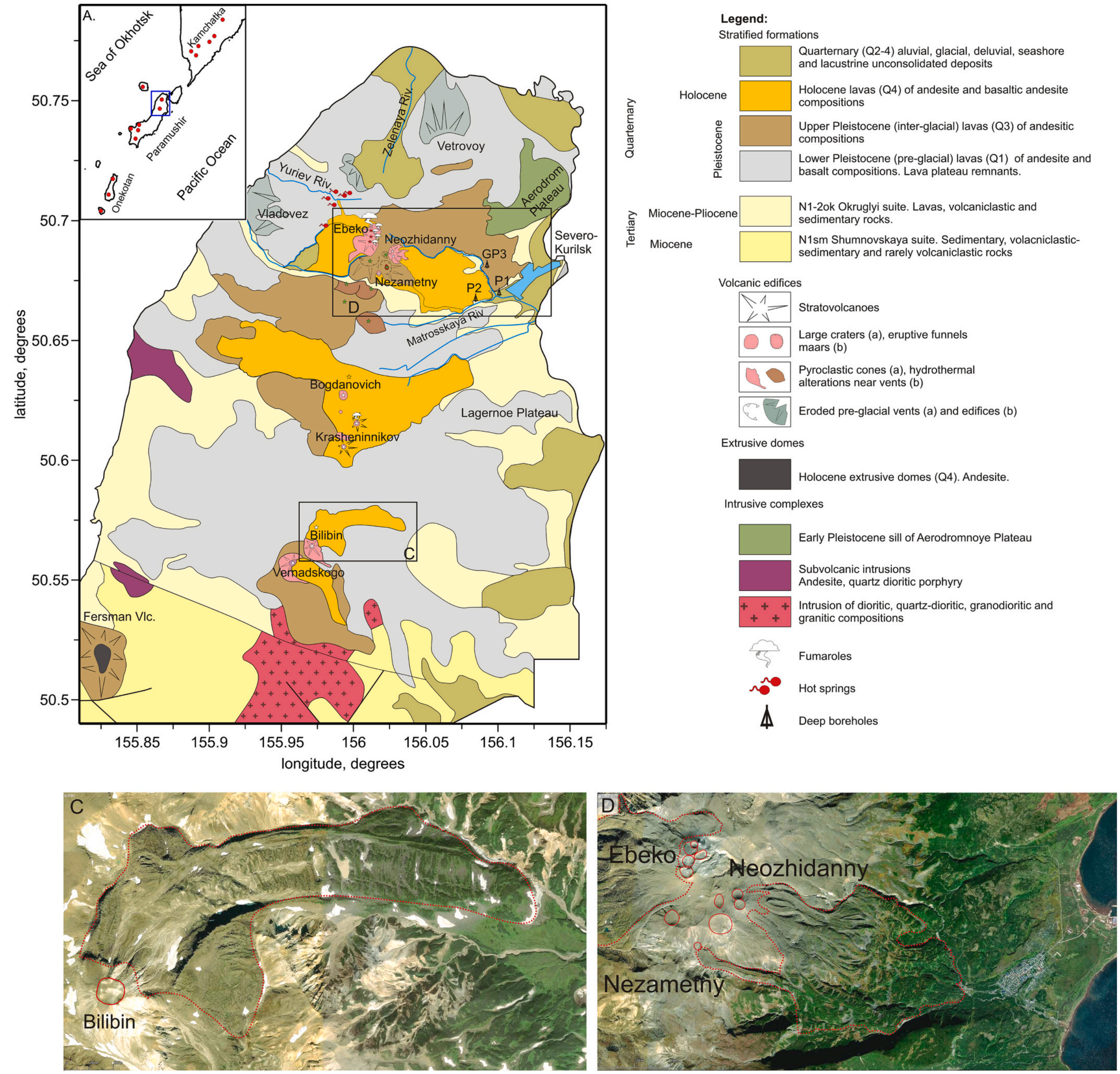

Fig. 1. Study area. A. Location of Paramushir Island. Red dots depict Holocene volcanoes. B. Geological map of Northern Paramushir after Melekestsev et al., (1993), State Geological Map, (2001) and corrected by the authors of this study. C and D are the satellite images of selected lava flows in areas indicated in B by rectangles (from ESRI ArcGIS Source). Red lines highlight the major lava flows and cones. (For interpretation of the references to colour in this figure legend, the reader is referred to the web version of this article.)

northern terrain into thick lava plateau. Some flows reached sea shores in the northern and western parts of the island (Gorshkov, 1970). This plateau and eruptive centers had been strongly overprinted by two Pleistocene glaciation episodes and recently only several remnant plateaus persist at the eastern and northern slopes of the ridge, e.g. Lagernoye plateau (Fig. 1B).

Another stage of volcanic activity occurred in the Late Pleistocene corresponding to the pre- and interglaciation periods. The eruptive centers of this stage are also confined to the Vernadsky ridge crest and are better preserved than the Early-Pleistocene ones. These centers erupted multiple lava flows, which covered much smaller areas than the Early-Pleistocene flows.

Holocene activity of the Vernadsky Ridge mostly occurred in three distinct volcano groups: Ebeko, Bogdanovich and Vernadsky, containing >40 eruptive centers (Gorshkov, 1970). The Vernadsky group is the southernmost group on the Vernadsky Ridge composed of Vernadsky and Bilibin volcanoes and several monogene centers. Vernadsky is the largest volcano having an altitude of 1183 m and the basement diameter of ~20 km. In the recent past, there were some massive effusive eruptions in this group, as evidenced by a large Holocene lava flow from Bilibin Volcano and a shorter flow directed from Vernadsky volcano, which are clearly identified in the satellite images (Fig. 1C).

The Bogdanovich volcano group located in the central segment of the Vernadsky Ridge consists of the dominating Kozyrevsky cone, less prominent Krasheninnikov and Bogdanovich cones and several more or less well preserved monogenic eruptive funnels and craters. The most recent lava flows propagate from Bogdanovich and Krasheninnikov vents along the eastern and western flanks of the ridge, respectively (Fig. 1B).

The Ebeko group is the youngest part of the Vernadsky Ridge. It is developed in the vicinity of strongly eroded early-Pleistocene Vetrovoy and Vlodavez volcanoes composing the northern edge of Paramushir Island. Large Holocene lava flows produced by Ebeko, Nezametny and Neozhidanny cones indicate a large effusive potential of this volcano complex (Fig. 1D). Ebeko is a complex volcano having an altitude of 1156 m and comprising three major craters with diameters of 250–300 m each (Fig. 1B and D). Most of the erupted products of Ebeko are composed of andesites and basaltic andesites. The juvenile material of the ongoing eruption represents highly crystalline and highly viscous ($>10^8$ Pa*s) low-silica (56–58 wt% SiO_2) andesite (Walter et al., 2020; Belousov et al., 2021). The ejected pyroclasts are variably vesicular bread-crust bombs, lapilli, and ash.

Ebeko is one of the most active volcanoes in Kuril Arc (Kalacheva and Voloshina, 2022). The eruptions of juvenile material (lava flows and pyroclasts) started on Ebeko in 420–200 BCE In the 17th–21th centuries all eruptions of Ebeko were phreatic and phreatomagmatic with supposed large-volume lahars (Melekestsev et al., 1993, 1994). In the 20–21 centuries, Ebeko Volcano erupted in 1934–1935, 1967–1971, 1987–1991, 2009–2011, and the 2016-ongoing. During the most recent activity phase, powerful phreatomagmatic eruptions occur regularly (Girina et al., 2019; Belousov et al., 2021; Kotenko et al., 2023). Special study by (Walter et al., 2020) demonstrated that in the summer of 2021, average time between individual explosions was 34 min. Kotenko et al. (2023) reported temporal gaps between individual explosions from 2 min to 3.5 h (average 58 min) in July 2022. In the cases of strongest eruptions, the height of the ash plume reached 5–7 km. The breadcrust bombs ejected during the ongoing eruptions (2019–2023) composed of highly crystalline low-silica (56–58 wt% SiO_2) andesites (Belousov et al., 2021; Kotenko et al., 2023). The ash ejected during this period contained vitreous juvenile material and had similar bulk composition while in 2022 silica contents of the ash decreased down to 52–56 wt% (Kotenko et al., 2023). Mineralogical observations on the ash particles suggest that these eruptions may have been caused by intrusions of magma into shallow water-saturated country rocks (Kotenko et al., 2023). However, the buoyancy of magma at this stage is not enough to produce lava eruptions and extrusions (Belousov et al., 2021).

In the summit area of Ebeko at an altitude of >1000 m, there are several fumarolic and solfataric fields and heated sites, which may change the locations very quickly (Fig. 1B). The temperature of gasses in the fumaroles in the summit area is generally low (<120 °C), but in some cases it may reach 500 °C (Kotenko et al., 2007). During the ongoing activity period, the total amount of ejected gasses from the main active crater and fumaroles is approximately 9000 tons per day (Rychagov et al., 2010). Emission of hot gasses with the temperature of up to 98 °C was observed on the extinct Krasheninnikov Volcano in the middle part of the Vernadsky Ridge (Kotenko and Kotenko, 2006).

Verkhne-Yuriev Springs is another thermal field on the western flank of Ebeko Volcano located at a distance of 2.5 km from the crater area at altitudes of 280–550 m (Fig. 1B). These springs discharge highly acidic and hot water with the temperature of up to 87 °C, forming the Yuriev River, which transports a large amount of dissolved matter to the Okhotsk Sea (Bortnikova et al., 2006; Kalacheva and Kotenko, 2013; Kalacheva et al., 2016). The daily amounts of ~60–80 t Cl make Yuriev Springs ranked among the sites with largest chlorine output in the world (Kalacheva et al., 2016). It is still debated whether the Ebeko's summit and Verkhe-Yuriev thermal fields are connected or not (Khubaeva et al., 2022).

Along the eastern slope of the Vernadsky Ridge, there are several highly-mineralized lower-temperature hydrothermal sources. Studies of the chemical and isotopic compositions of solfataric gasses in different sites of Paramushir have been carried out since 1957. Based on the results of geochemical studies, there are both sea-water and fresh groundwater aquifers above a shallow magma reservoir serving as a powerful heater (Menyailov et al., 1985). According to the geochemical analysis of the thermal water and gases, there are near-surface local aquifers under Ebeko Volcano too (Kalacheva et al., 2016; Kalacheva and Voloshina, 2022).

Despite a large number of multidisciplinary studies, the deep processes causing magmatic and hydrothermal activity on Paramushir remains poorly understood. The data collected by the temporary seismic network in 2021–2022 give a possibility for the principal advance in studying the magma plumbing systems below volcanic complexes in the Northern part of Paramushir.

3. Data and algorithms

We deployed a temporary seismic network composed of 21 seismic stations equipped with broadband three-component sensors Guralp CMG-6 T (with periods of up to 30 s) from June 2021 to June 2022 (Fig. 2a). In addition, we used the data from the permanent seismic station SKR installed in Severo-Kurilsk and equipped with the sensor Guralp CMG-3 TB (up to 120 s period). In all cases, the recording was conducted with the sampling rate of 100 Hz. Unfortunately, some stations got out of order due to animal attacks (bears, foxes) and flooding. For example, station VER19 was broken three days after the start date and was not used in the analysis. The majority of other stations gradually got out of order during the network operation, as shown in Fig. 2b. For this reason, the numbers of the daily cross-correlations were different at different station pairs ranging from one to eleven months.

We computed ambient seismic noise cross-correlation functions (CCF), to obtain the inter-station Rayleigh surface waves dispersion curves, which included the steps (Bensen et al., 2007):

1. Band-pass pre-filtering of all daily seismic traces in the period range 0.2–30 s;
2. Removing of the instrument response;
3. Detrending and demeaning of the records;
4. Band-pass filtering in the period range 0.25–30 s;
5. Down-sampling from 100 Hz to 10 Hz to reduce the amount of the data;
6. Running absolute mean normalization as time-domain normalization;
7. Spectral whitening with spectral windowing in the period range 0.25–30 s, applying it to 2-h slices of records;
8. Cross-correlation of 2-h slices with the step of 1 h;
9. Linear staking of all daily CCF for each station pair in the available time interval.

Before applying all filters and Fourier transform in all steps, the seismic signals were tapered.

Fig. 3a shows an example of the vertical-vertical CCF for the pair of stations SKR and VER12 with the presentation of the daily CCFs. It can be seen that the CCFs are regularly shifted relative to the zero point during the observation period. As a result, the daily CCFs are not summed coherently as can be seen in the bottom panel in Fig. 3a. This shift indicates that at least at one station, the communication with GPS satellites was lost, and it caused loss of clock synchronization and gradual accumulation of the internal clock time errors (Sens-Schönfelder, 2008). Only three seismic stations (VER02, VER11, VER12) have the time errors. We cannot use a method based on a reference cross-correlation function because most daily CCFs have a time shift. So, we decided to apply a method without the reference CCF (Belovezhets et al., 2022). First, we applied denoising CCFs based on the singular value decomposition with Wiener filtration (Moreau et al., 2017). Second, we computed Pearson correlation coefficients (Hable et al., 2018) and associated time-shifts between all daily CCFs. Then for correlation

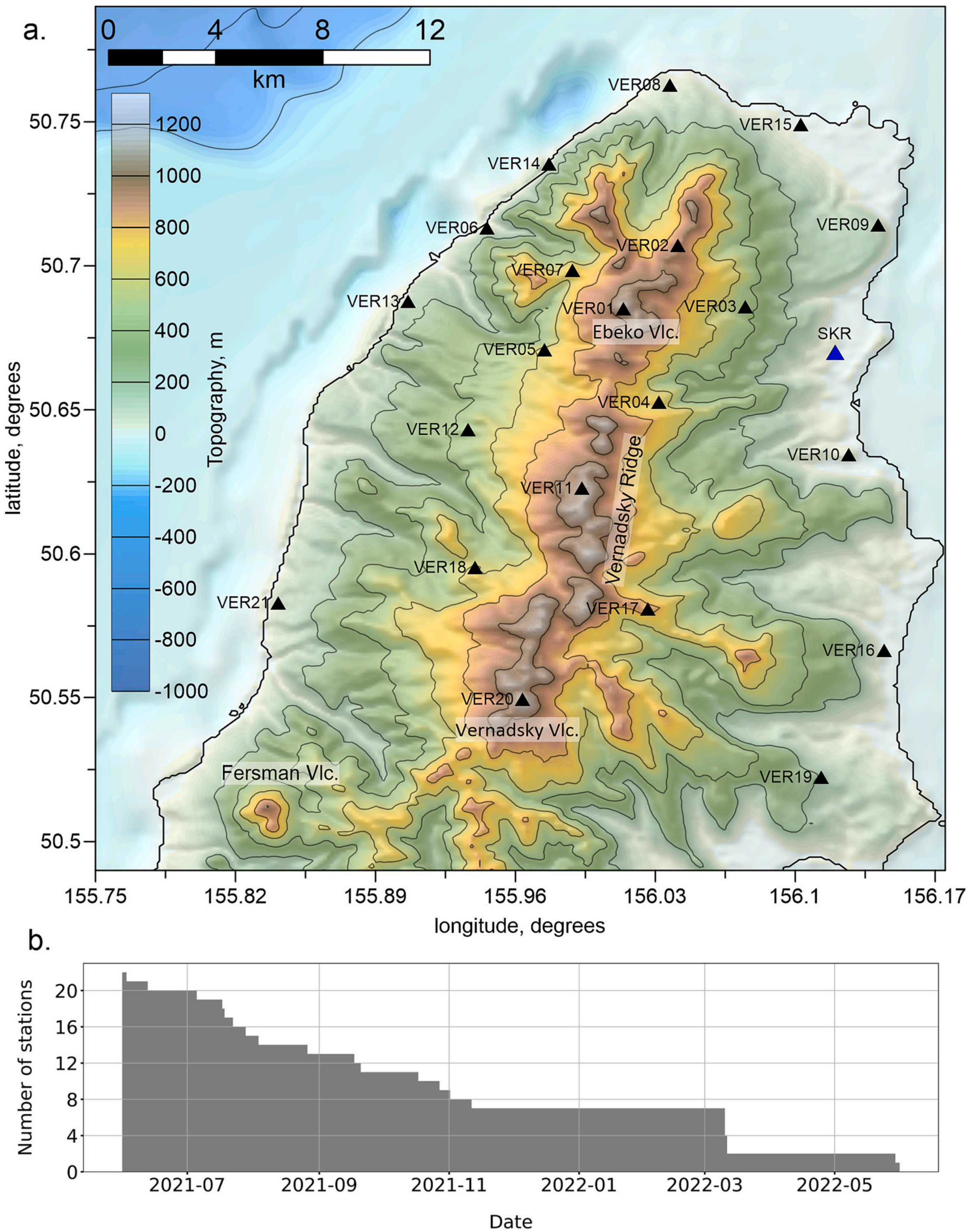

Fig. 2. Temporary seismic network configuration. a.Topography map in the study area with the location of the seismic network in the study area. The gray contour lines indicate the topography with the interval of 200 m. The black triangles are the temporary stations installed in 2021–2022 and the blue triangle is the permanent station by KB GS RAS. b. Graph with availability of data from the stations during the entire period of the network operation. (For interpretation of the references to colour in this figure legend, the reader is referred to the web version of this article.)

coefficients at a single pair of stations we used the Monte Carlo Markov Chain (MCMC) approach as suggested by Taylor and Hillers (2020) to estimate the clock drift and correct every raw (before denoising) CCFs. Also we applied denoising CCFs based on the singular value decomposition with Wiener filtration (Moreau et al., 2017) after the clock correction. In Fig. 3 (b) an example of filtered and corrected CCF is shown.To increase the quality of the data we use signal-to-noise (SNR) criteria – every daily CCF should have SNR to be >10 to be averaged. The corrected CCFs are presented in Fig. 3b. It can be seen that they are stacked coherently and reveal a clear Green function in the CCF.

We applied Frequency Time Analysis (FTAN) to the ZZ-components of the CCFs (Dziewonski et al., 1969; Levshin et al., 1989) to measure

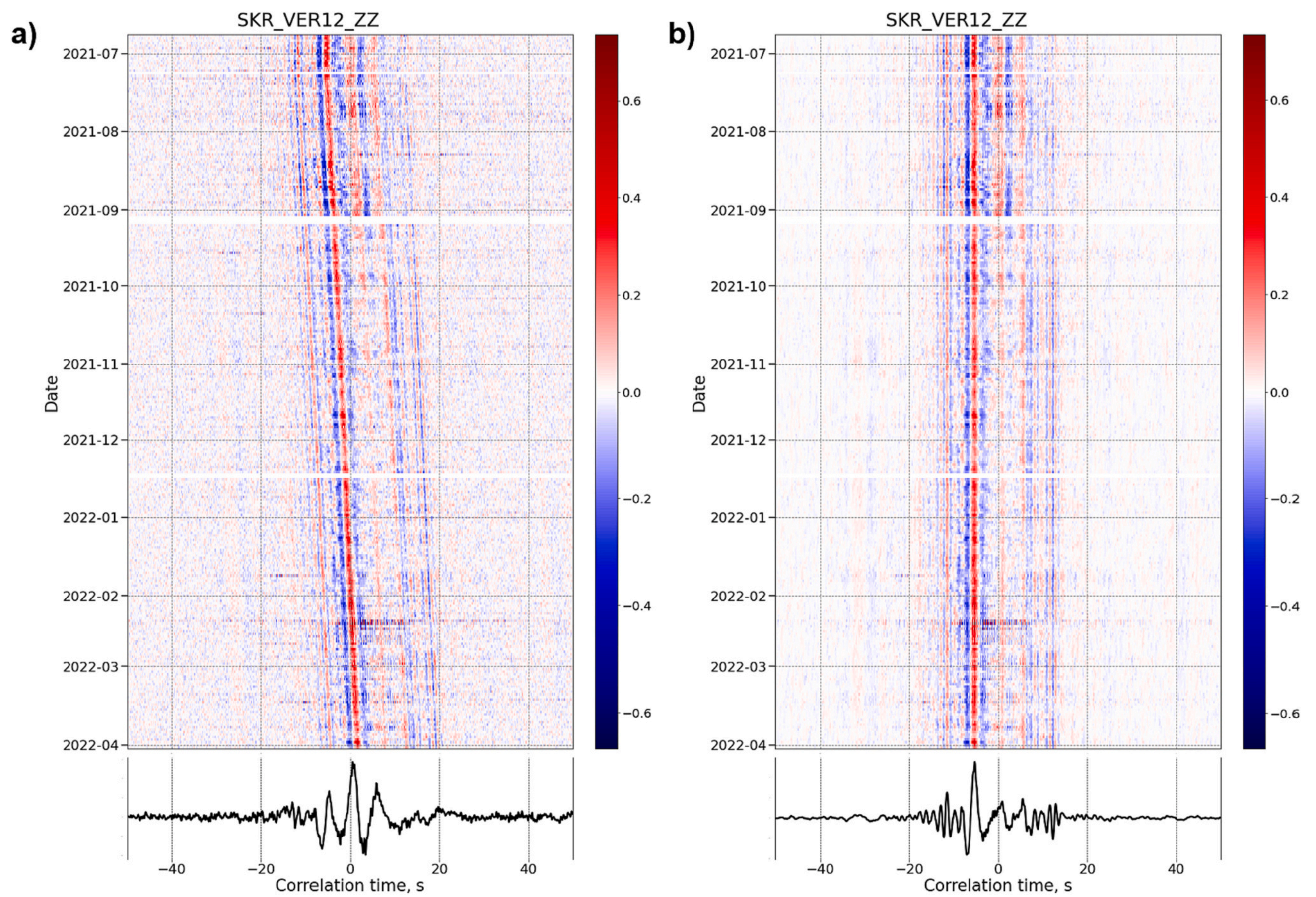

Fig. 3. Cross-correlogram for stations SKR and VER12 for vertical components (a) - before time-correction, (b) - after denoising and time-correction. The upper panels show the composite plots of daily cross-correlation functions and the lower graphs present the stacking results for the entire observation period.

the interstation Rayleigh wave group velocity dispersion curves. Fig. 4 a, b shows two examples of FTAN for two pairs of stations, representing the normalized energy of CCF filtered in a series of narrow-band filters. The high-energy zone clearly indicates the dispersion of the Rayleigh surface wave fundamental mode. As the number of interstation pairs was not very high, we visually examined the quality of each CCF and manually picked the dispersion curves by following the energy maxima and avoiding abrupt jumps in group velocity variations. We separately picked group velocity dispersion curves based on the left and right sides of CCF, as well as on the stacked CCF on both sides. Although in some cases, the dispersion curves for the same source-receiver pair differed significantly, they were all used in the least squares inversion procedure. In this case, possible outliers were removed during the tomography step. The dispersion curves were picked from the smallest period of 0.5 s. The largest period was defined according to the interstation distance corresponding to one wavelength with the average group velocity of the Rayleigh wave in the crust (2 km/s). For stations located on the opposite sides of the network the largest period reached 12 s. Fig. 4c presents the distributions of all manually picked dispersion curves. It can be seen that they vary in a large range of group velocities indicating that the structure beneath the study area is highly heterogeneous. Same conclusion follows from the initial FTAN analysis in Fig. 4a,b. It can be seen that for the station pair SKR-VER12, the group velocities at periods of 0.5–2 s is between 1000 and 1500 m/s, whereas for the pair of VER02-VER17, the velocity in the same interval of periods is between 1800 and 2000 m/s. In the latter case, the ray path travels along the western flank of the Vernadsky Ridge, implying high velocity at shallow depths.

The derived dispersion curves are used as input files for the two-step tomography inversion with the use of the SURF_TOMO code (Koulakov et al., 2016) to compute the 2D group velocity maps (first step) and then to derive the 3D shear-wave velocity model (second step). The 2D group velocities are calculated for the periods ranging from 0.5 to 12 s with the step of 0.5 s. The number of rays for different periods varied from 383 to 11. The 2D tomography inversion was performed iteratively. The average constant group velocity for each frequency was used as a starting model. The rays were traced using the bending method taking into account the topography and velocity heterogeneities after updating the velocity model (see an example for one period in Fig. 5a). The parameterization nodes were defined regularly with the step of 1 km in areas with sufficient ray coverage (>0.1 of the mean ray density), as shown in Fig. 5b. Between the nodes, the velocity is approximated using the bi-linear interpolation. The inversion was performed using the least-square algorithm with QR normalization, LSQR (Paige and Saunders, 1982; Nolet, 1987). The solution stability was controlled using the smoothing and amplitude damping terms, which were included with the coefficients of 6 and 3, respectively. In total, for the stage of 2D group velocity calculations, we performed three iterations. The distributions of group velocities for selected frequencies are presented in Fig. 6.

The resulting 2D group velocity distributions at different frequencies were used to obtain the mean dispersion curve (blue line in Fig. 7c), which was then converted to the reference 1D distribution of Vs. To perform this conversion, we calculated sensitivity kernel A_{ij} showing the deviation of group velocity at the i-th period due to the unit S-wave velocity variation in the j-th depth interval (Fig. 7a). The forward modeling (calculation of group velocity based on the given 1D S-wave velocity distribution) was performed using the algorithms developed by Herrmann (1987). Besides the S-wave velocity, this code requires the distributions of the P-wave velocity and density; however, they have minor effects on the group velocities. Therefore, in our case, they were defined in a simplified way: the Vp was calculated from Vs using a

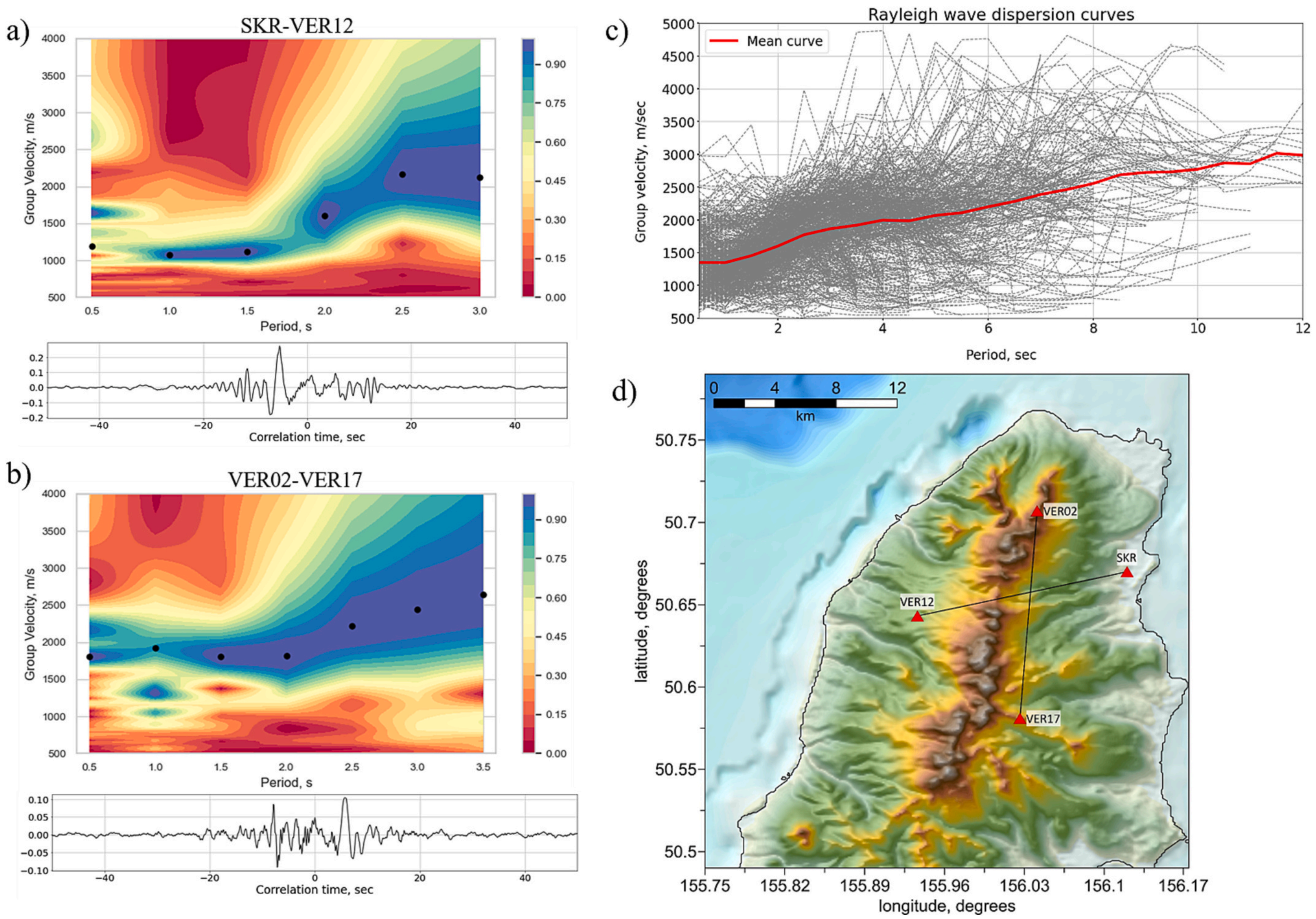

Fig. 4. Measurements of the dispersion curves of the interstation Rayleigh wave group velocities. (a, b) FTAN amplitude diagrams for the cross-correlation functions plotted below. The black dots indicate the picked group velocities. (c) Composite plot with all manually picked dispersion curves; the red line is the mean dispersion curve. (d) Map showing the station pairs used for presenting the dispersion curves in a and b. (For interpretation of the references to colour in this figure legend, the reader is referred to the web version of this article.)

constant value of Vp/Vs = 1.7, and the density was presumed to be equal to Vs. To approximate the target 1D velocity model, the parameterization nodes were distributed uniformly with the spacing of 0.5 km. The inversion was performed using the LSQR algorithm with implying smoothing and amplitude damping. After computing the 1D model, the new sensitivity kernels and updated residuals were calculated, and then inverted into the next 1D velocity model. In total, to calculate the final reference 1D velocity model, we performed five iterations. The sensitivity kernels and results of the 1D model optimization for the average model are shown in Fig. 7.

To derive the 3D model of shear-wave velocities, we calculated the local dispersion curves for every parameterization node, where at least one value of group velocity was calculated. For every node, we calculated the sensitivity kernels, similarly as described in the previous paragraph, and group velocity residuals. The inversion was performed using the LSQR algorithm for all nodes simultaneously attributing smoothing between the nodes in horizontal and vertical directions. After inversion, the updated 3D Vs model was used to calculate the new sensitivity kernels and residuals. In total, the final 3D velocity model was calculated after two iteration steps.

To assess the resolution of the derived model for our data configuration, we performed several synthetic tests. The synthetic model was defined as a superposition of the reference 1D velocity and 3D anomalies. Based on the three-dimensional synthetic model, using the Herrmann (1987) algorithm, we calculated the 2D group velocity distributions for different periods. Then for the same pairs of stations as exist in the experimental dataset, we calculated the synthetic travel times in the derived 2D group velocity models using the bending ray tracing algorithm. This synthetic dataset is used as an input for the same tomography workflow as was implemented to process the experimental data. The recovery results are compared with the actual distribution of synthetic structure, which gives an idea about spatial resolution of the inversion. Fig. 8 presents an example of the recovery of the checkerboard model with alternated positive and negative anomalies having the size of 8x8x5 km and amplitude of ±8%. It can be seen that the anomalies in this model are correctly recovered in three layers down to the depth of at least 10 km.

4. Results and discussion

The main result of this study is the model of 3-D S-wave velocity distribution beneath the northern part of Paramushir Island derived from ambient noise tomography. In Fig. 9 the deviations of the S-velocity with respect to the average 1D model are given in four depth levels. Note that in this case, the depths are measured with respect to the surface, therefore the visualization levels are parallel to topography. Fig. 10 presents the distribution of the velocity anomalies and absolute shear-wave velocity in three vertical sections. As inferred from the checkerboard test, we can robustly recover the seismic velocity heterogeneities to at least 7–10 km depth. The schematic interpretation of the derived distributions of the velocity anomalies is presented in Fig. 11.

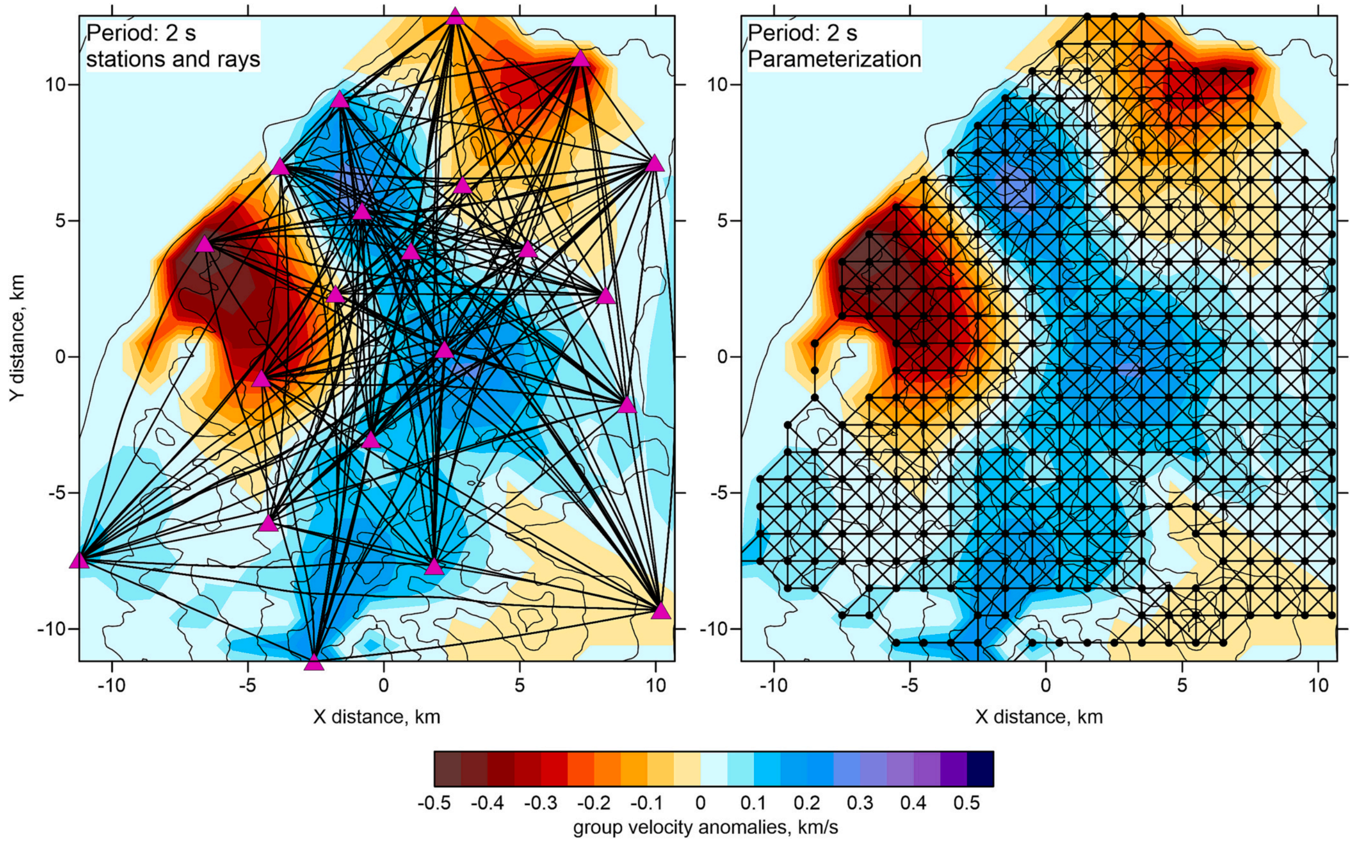

Fig. 5. Example of ray tracing and grid construction. Background is the result of inversion for group velocity at 2 s period after three iterations. The left panel shows the final ray paths (black lines) and stations (magenta triangles). The right panel demonstrate the parameterization nodes and links used for smoothing. The thin contour lines on background represent the topography. (For interpretation of the references to colour in this figure legend, the reader is referred to the web version of this article.)

4.1. *High-velocity rigid cover of Vernadsky Ridge*

The most prominent feature of this model is the high-velocity anomaly below the Vernadsky Ridge at shallow depths. This anomaly is visible in the group velocity maps at periods of 1 s, 2 s and 3 s (Fig. 6). Approximately the same shape of the high-velocity anomaly is observed in the distributions of S-wave velocity anomalies in horizontal sections at 0.5 and 2 km depth (Fig. 9). This anomaly seems to consist of two isolated parts. The southern part follows the southern segment of the Vernadsky Ridge and includes the volcanic centers Vernardsky, Bilibin, Krasheninnikov and Bogdanivich. In the northeastern side, this anomaly covers the Lagernoe Plateau. The northern high-velocity anomaly starts at Ebeko Volcano and propagates northwest roughly along the Yuriev river. It also includes parts of extinct Vlodavez and Vetrovoy volcanoes, which might have the common basement.

The high-velocity anomalies associated with a volcano edifice is a rather typical feature observed in tomography models for many volcanoes in the world, such as Vesuvius (Zollo et al., 1998), Mt. Etna (Díaz-Moreno et al., 2017), Ushkovsky in Kamchatka (Koulakov et al., 2020) and Teide in Tenerife Island (Koulakov et al., 2023). In all these cases, the high-velocity anomalies within volcano edifices were interpreted as highly consolidated cover gradually formed during volcano evolution (Christensen, 1996). We propose that the same interpretation is valid for the volcanic centers along the Vernadsky Ridge. In the southern part of the Vernadsky Ridge, the prominent shallow high-velocity anomaly may indicate the location of the solidified rigid body beneath the group of Vernadsky and Bilibin volcanoes. Such a body is prominent in the State Geological Map sheets M-56-XII, XVII, XVIII and XXIV (State Geological Map, 2001). According to the supplementary materials to the Map, this body is Prozrachnensky massif, composed of granite-granodiorites and diorite-quartz diorites. It is well exposed to the south of the study area (Fig. 1B). However, in the deep valleys upstream of Zaozernaya river, running from the SE flank of Vernadsky volcano to the Sea of Okhotsk, the diorite-quartz diorites of this massif, outcrop beneath its lava flows (Fig. 1B), indicating that the massif continues northward under their cover. As follows from our tomography, this upper crustal body may reach Krasheninnikov and Bogdanovich volcanoes.

It can be seen that the shallow high-velocity anomalies beneath the northern and southern segments of the Vernadsky Ridge appear to be separated by a zone of relatively low velocity, which corresponds to local lowering on the Ridge. This implies that the northern and the southern groups of volcanoes on the Vernadsky Ridge turn out to be isolated and may have developed independently, or have been differently modified by hydrothermal activity since then (Heap et al., 2021).

4.2. *Low-velocity magma sources below Vernadsky Ridge*

At larger frequencies and at larger depths, the anomalies appear to be reversed with respect to the shallow structures: a prominent latitudinally oriented low-velocity anomaly is observed along the Vernadsky Ridge and it is surrounded by high-velocity anomalies below the eastern and western flanks. The checkerboard test in Fig. 8 has demonstrated the capacity of the tomography with the present dataset to robustly recover this transition. Note also that this velocity reversal could be predicted from the result of the 1D velocity optimization showing slight S-wave velocity decrease at depths of 4–5 km (Fig. 7).

This low-velocity anomaly along the Vernadsky Ridge at 6 km depth appears to be not homogeneous. There are at least two anomaly maxima, one of which is located below the Vernadsky and Krasheninnikov volcano clusters, and another one is associated with the Ebeko group. It can

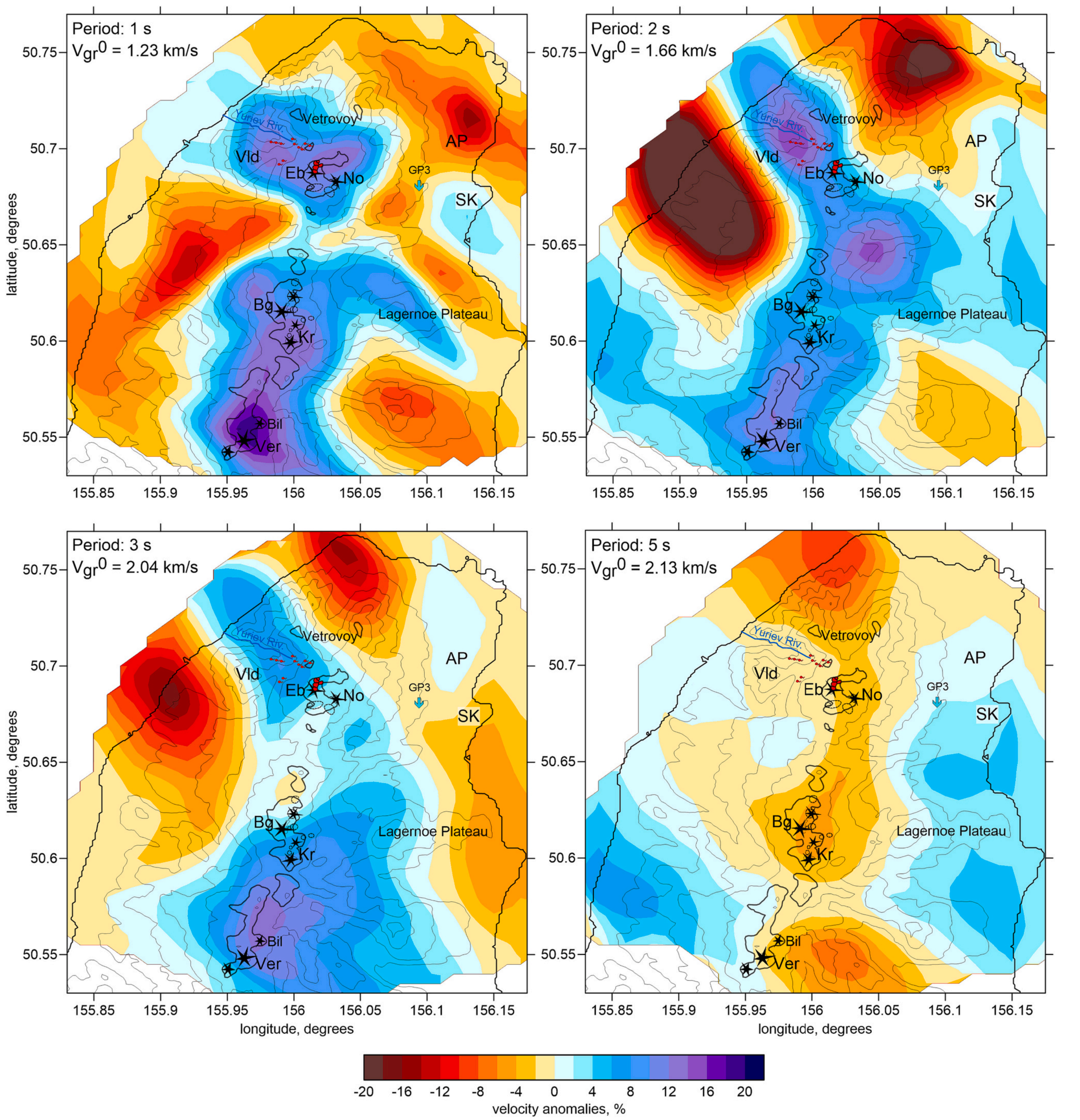

Fig. 6. Anomalies of the group velocities at four periods. The mean group velocities and periods are indicated in the top-left corners of the plots. The gray contour lines indicate the topography with the interval of 200 m, and the thick black line highlights the level of 1000 m. The blue arrow indicates the deep borehole. The black stars and ellipses indicate the main volcanic complexes and cones with abbreviations: Ver - Vernadsky; Bil - Bilibin; Kr- Krasheninnikov; Bg - Bogdanivich; Eb - Ebeko; No - Neozhidanny; Vld - Vlodavez. AP is Aerodrom Plateau. The active craters of Ebeko are highlighted with red. (For interpretation of the references to colour in this figure legend, the reader is referred to the web version of this article.)

be seen in vertical sections of absolute velocities (right column in Fig. 10) that the low-velocity anomalies are located at 4–6 km depth. These low-velocity anomalies likely represent two large reservoirs of eruptible magma below the Vernadsky Ridge that are responsible for the Holocene volcanic activity in this area.

The southern low-velocity anomaly appears to be stronger and larger, although it is located below the volcanoes that are presently not active. This observation can be explained by the existence of a large high-amplitude positive velocity anomaly at shallower depths that probably represents a rigid granodiorite cover that prevents magma to ascend. At the same time, in the geological map and in satellite images, we can observe massive lava flows from the cones of Vernadsky, Bilibin, Bogdanovich and Krasheninnikov in this part of the ridge covering large areas and propagating to large distances (Fig. 1). It shows that episodically magma from the reservoir at 4–6 km depth finds ways to the surface through the rigid cover, which results in large effusive eruptions. Such magma pathways below the southern part of Vernadsky Ridge are schematically depicted with purple veins in Fig. 11. A very similar

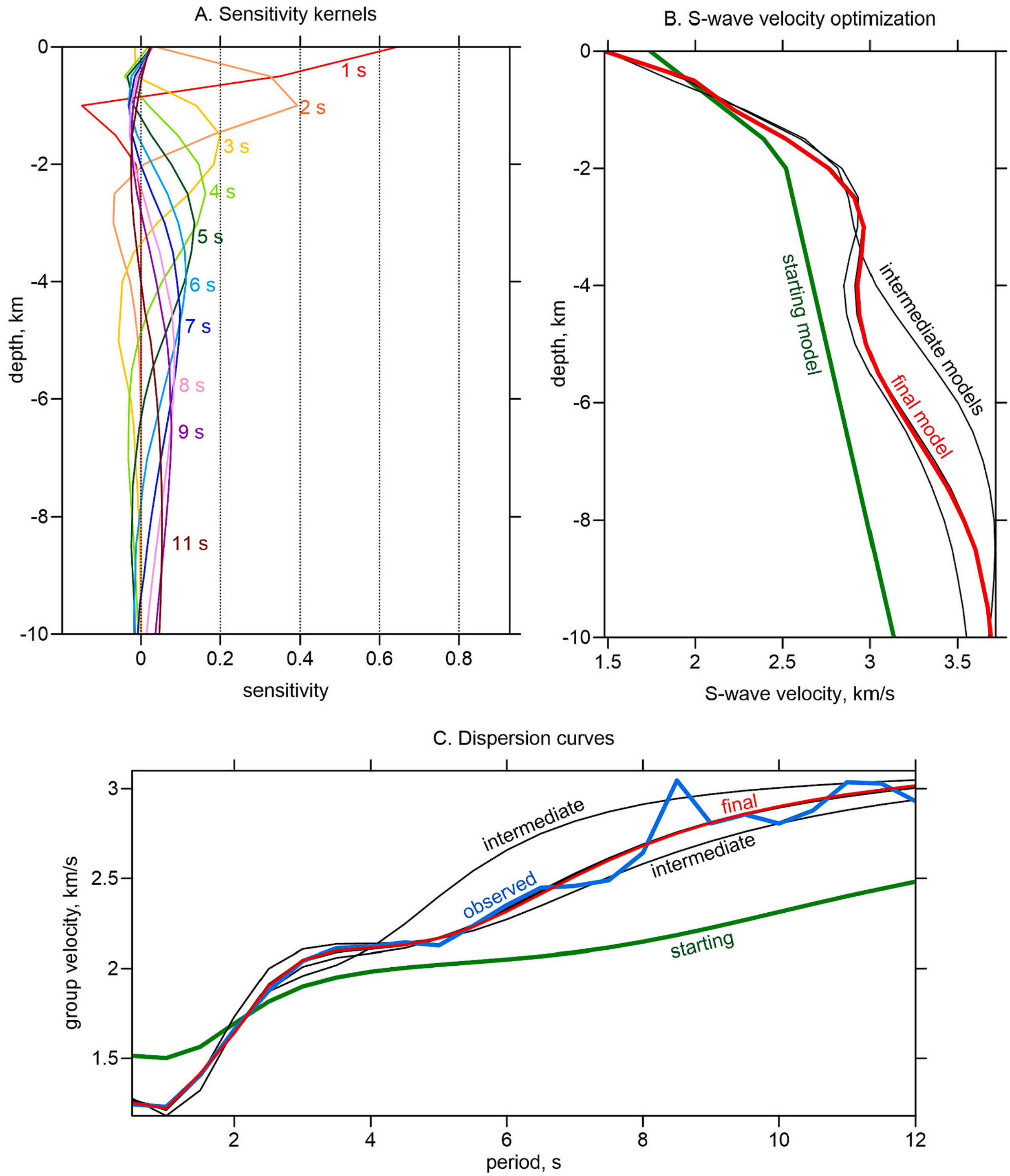

Fig. 7. Optimization of the 1D velocity model. A. Sensitivity kernels for different periods indicated by different colors. B. Velocity distributions for the starting model (green), intermediate (black) and final (red) models. C. Dispersion curves corresponding to the observed data (blue), starting model (green), intermediate (black) and final (red) models. (For interpretation of the references to colour in this figure legend, the reader is referred to the web version of this article.)

scenario was realized in the recent eruption of Cumbre Vieja Volcano on La Palma in 2021 (D'Auria et al., 2022). In that case, magma accumulated for a long time in a deep reservoir, and after reaching a critical pressure, it fractured the rigid brittle cover and quickly ascended to the surface. The volume of the lava flows on La Palma is compatible with those on the southern segment of the Vernadsky Ridge on Paramushir.

Below Ebeko, we observe a smaller low-velocity anomaly likely representing a magma reservoir at 4–6 km depth overlain by the high-velocity anomaly. It looks smaller and less intensive than the anomaly below the southern part of the Vernadsky Ridge. Therefore, below Ebeko, it might be more permeable for ascending magmas and fluids. In this case, there might be some pathways (dikes, sills) that presently deliver magma upward, as schematically depicted by the red veins in Fig. 11. However, the total volume of these hot magma bodies is relatively small and they cannot be resolved by our tomography model; they just have an integral effect by lowering the amplitude of the high-

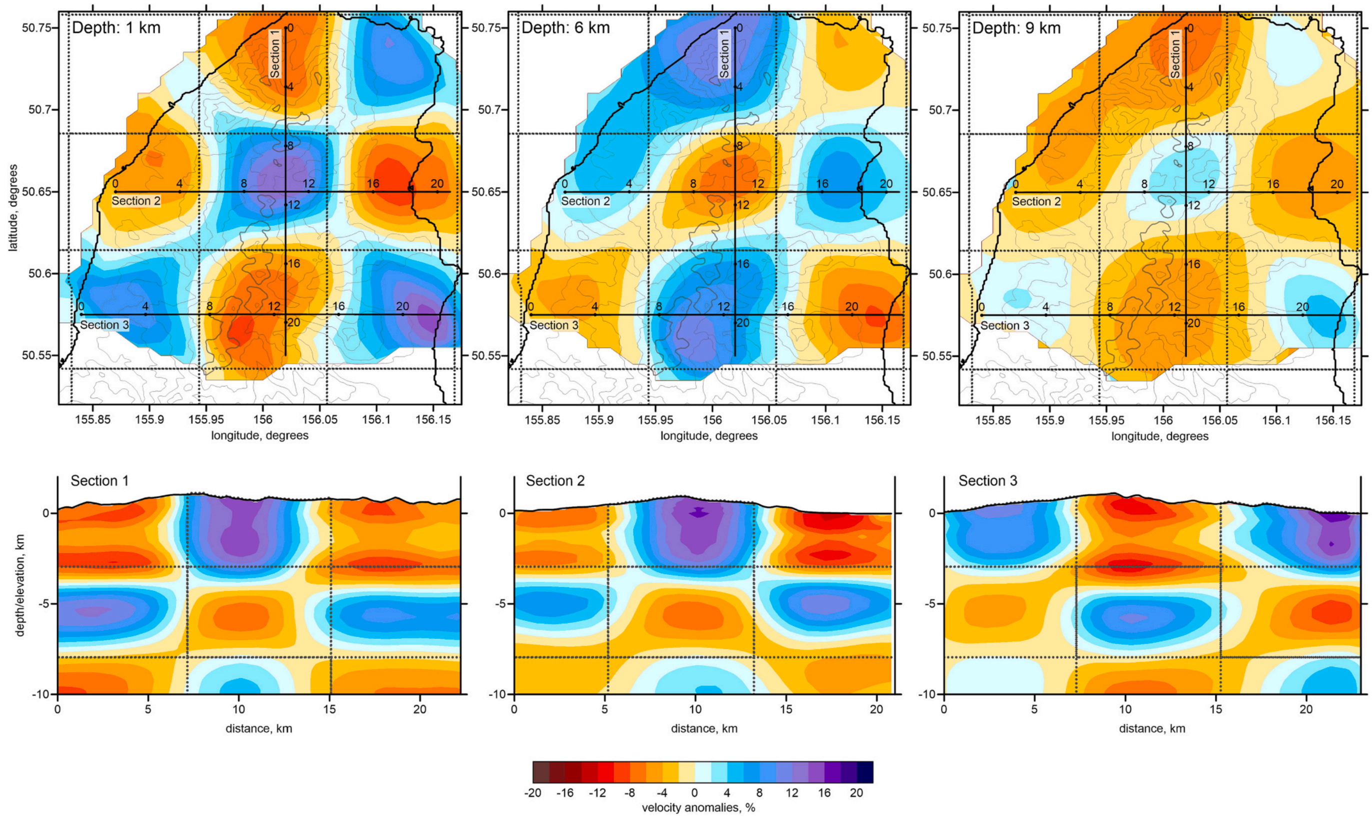

Fig. 8. Checkerboard test. The recovery results are shown in three horizontal and three vertical sections. The locations of the profiles are indicated in maps. The dotted lines indicate the shapes of the synthetic anomalies. In the maps, the gray contour lines indicate the topography with the interval of 200 m, and the thick black line highlights the level of 1000 m.

velocity anomaly in the rigid cover. This is consistent with the general concept of eruption mechanisms of Ebeko proposed by Belousov et al. (2021). In their final conceptual scheme, they hypothesized that the top of the main magma storage is located at approximately 5 km depth. Above this storage, they presume the existence of small diapirs that slowly ascend due to their positive buoyancy. When crossing water- and sulfur-bearing layers (blue lenses in Fig. 11), they produce a large amount of gasses that ascend to the surface and exit from the active vent of Ebeko and summit fumaroles.

Another hypothesis could associate the observed low-velocity anomalies below 6 km depth with storages of hydrothermal fluids. However, if these fluids are of meteoric origin, it is very unlikely that they can reach such depths. According to McIntosh and Ferguson (2021), the meteoric fluid circulation may theoretically reach the depth of 5 km; however, in this case, the fluid concentrations in deeper layers is dramatically lower than in the shallower parts. Therefore, we do not believe that meteoric fluids are capable of forming such voluminous reservoirs, as we observe in our tomography model. An alternative could be the presence of juvenile fluids that arrived from the dehydrated slab and mantle wedge. In this case, the most probable migration method of such fluids is transportation in a dissolved form together with ascending magmas. In this case, the anomalies that we observe in our tomography model may indeed contain some juvenile fluids, but they are stored in large magmatic reservoirs.

4.3. *Traces of aquifers and shallow sediments*

Another interesting feature that can be observed in Fig. 10 is a thin nearly horizontal low-velocity layer located at a depth of ~1 km, which is most clear below the eastern flank of Ebeko in Section A3-B3. It might represent a water-saturated layer that connects the Ebeko hydrothermal system with the Pacific coast area. Such an aquifer was predicted by different authors (e.g., Kalacheva et al., 2016; Rychagov et al., 2002). However, no aquifer was revealed by the deep drilling in the GP3 borehole reaching the depth of 2500 m (Belousov et al., 2002; Rychagov et al., 2002). As shown in Section A3-B3, this borehole gets to the location, where the aquifer-related anomaly almost disappears. It may indicate that the borehole crossed the location where the existence of the aquifer is less probable. To the left of the borehole in Section A3-B3, we observe a low-velocity anomaly that seems to be connected with the magma reservoir anomaly. It might represent a magma and/or fluid pathway, possibly associated with a fault zone schematically depicted by thin lines in Fig. 10 at 10–12 km of Section A3-B3. Note that a fault in this location was identified by Khubaeva et al. (2022). Our results infer that the GP3 borehole was drilled in a wrong location, where the probability of geothermal resources is minimal. Moving it up or down to a few hundred meters along the slope would likely increase a chance to get to a hot-water-bearing layer suitable for geothermal exploration.

The similar low-velocity layer is observed in Section A1-B1 between Krasheninnikov and Ebeko Volcanoes. The top of the Vernadsky Ridge is covered by a non-permeable layer consisting of lava flows. At the same time, according to our field observations, between Bogdanovich and Ebeko volcanoes, there is an elongated zone of hydrothermally altered rocks that might be associated with a regional fault. This fault appears to be associated with valleys of the Gorshkov and Matrosskaya rivers and it was indicated in the State Geological Map (2001). Highly permeable, strongly altered rocks along this fault might serve as a pathway for meteoric fluids that penetrate to depths of up to 1.5 km below surface, as follows from the shape of the low-velocity anomaly in this zone (Section A1-B1 in Figs. 10 and 11). Our result clearly shows that fluids in this zone are directed southward to Krasheninnikov Volcano, where they may get in contact with remaining hot magma bodies and cause active

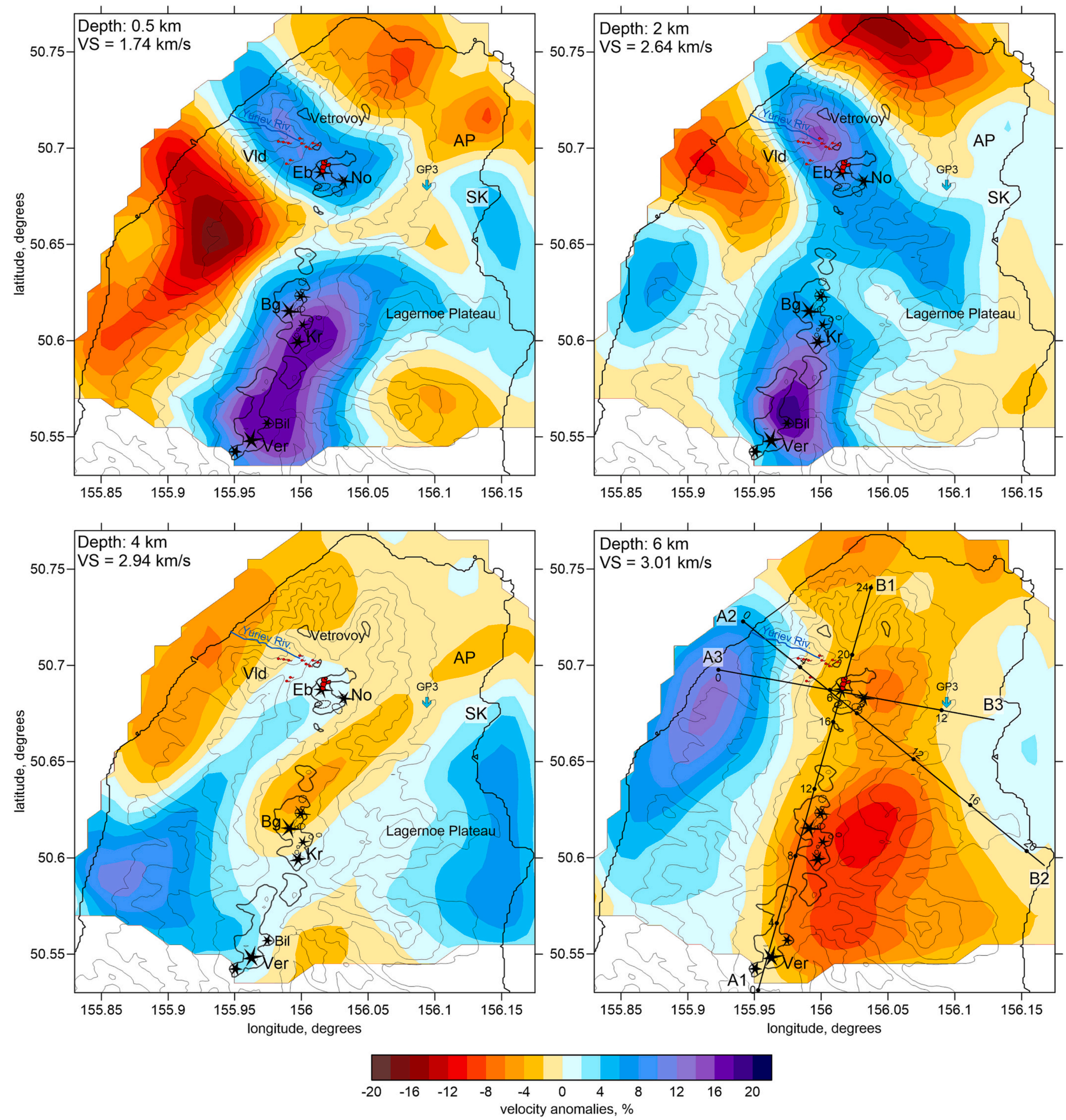

Fig. 9. Anomalies of the S-velocity model in four depth sections. The reference velocity values and depths are indicated in the top-left corners of the plot. The gray contour lines indicate the topography with the interval of 200 m, and the thick black line highlights the level of 1000 m. The blue arrow indicates the deep borehole. The black stars and ellipses indicate the main volcanic complexes and edifices with abbreviations: Ver - Vernadsky; Bil - Bilibin; Kr- Krasheninnikov; Bg - Bogdanivich; Eb - Ebeko; No - Neozhidanny; Vld - Vlodavez. AP is Aerodrom Plateau. The active craters of Ebeko are highlighted with red. The locations of the vertical sections are shown in the map at 6 km depth. (For interpretation of the references to colour in this figure legend, the reader is referred to the web version of this article.)

degassing (Fig. 11). This could explain episodic fumarole activity observed in this volcano cluster (Kotenko and Kotenko, 2006).

It should be taken into account that the relationships between faulting, hydrothermal alteration of rocks and permeability might be not obvious. For example, as shown by Heap et al. (2021), in some conditions, alteration might abruptly decrease permeability that might increase fluid pressure inside active volcanoes. In our opinion, this scenario is not valid for Ebeko and surroundings, as it exhibits almost permanent strong gas emission demonstrating that the ongoing fluid currents do not cause closing pores, as suggested by Heap et al. (2021). Active faults in most cases are presumed to be more permeable for fluids (e.g., Gudmundsson, 2000); however, in some cases of high fluid

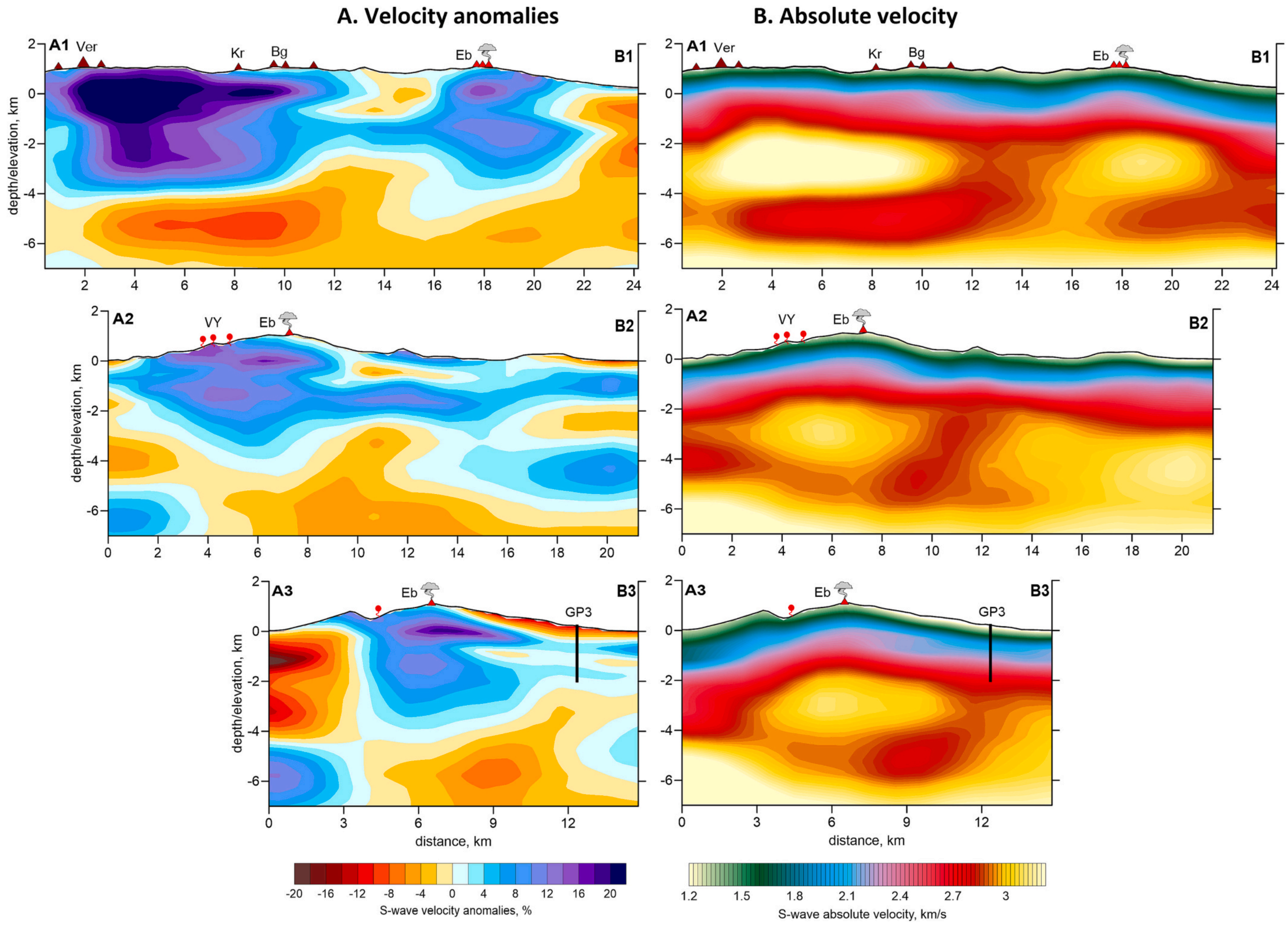

Fig. 10. Resulting 3-D shear-velocity distribution in three vertical sections, whose locations are indicated in Fig. 8. The left and right columns show the anomalies and absolute velocity distributions, respectively. The thick black line indicates the deep borehole. The red triangles indicate the main volcanic centers with abbreviations: Ver - Vernadsky, Kr- Krasheninnikov, Bg - Bogdanovich; Eb - Ebeko. Verkhne Yuriev Springs are indicated with VY. (For interpretation of the references to colour in this figure legend, the reader is referred to the web version of this article.)

mineralization and low displacement rates, the permeability in fault zones might decrease.

In the uppermost part of Section A3-B3 in Fig. 9, we can observe a thin low-velocity anomaly located along the eastern slope of Ebeko. We propose that it may represent a layer of strongly disintegrated rocks formed due to glacial erosion of pre- and inter-glacial lava flows. Some additional soft material might be accumulated due to pyroclastic flows whose traces were recorded by Melekestsev et al. (1993, 1994). These highly permeable rocks are strongly saturated by meteoric water coming from very active precipitation and ice melting. These factors give strong seismic velocity reduction down to a few hundred meters depth.

5. Conclusions

In this study we present the first crustal-scale shear-wave seismic velocity model of the northern part of Paramushir using the data recorded in 2021–2022 by the temporary seismic network and one permanent seismic station. We computed ambient seismic noise cross-correlation functions to obtain the Rayleigh wave group velocity dispersion curves and then used them by the ambient noise tomography. We performed synthetic tests that confirmed fair resolution of our tomographic results down to 7–10 km depth.

Along the volcanic Vernadsky Ridge, we obtain the low-velocity anomaly at the depth of 4–6 km associated with magma reservoirs, which is overlaid by a prominent high-velocity anomaly representing the rigid cover. The most prominent anomalies are observed below the southern and central segments of the Vernadsky Ridge, where no present volcanic activity is identified, but there are traces of massive Holocene lava flows. Thus, the presence of a large rigid cover prevents the continuous feeding of the volcanoes and leads to accumulation of large volumes of high-pressured magma that episodically come out to the surface during large effusive eruptions. Below Ebeko, the intensity of the anomalies is not as strong, which may indicate that the cover is not as resistant in this case and it allows for continuous ascent of magma intrusions leading to the long-term continuous eruption activity.

At a depth of ~1 km, we observe a thin, nearly horizontal low-velocity anomaly that may represent a water-saturated layer. Below Ebeko it may get in contact with ascended hot magma bodies and may produce a large amount of steam coming out during frequent phreatic eruptions of Ebeko and continuous fumarole activity in the summit area. This aquifer layer is traced along the eastern flank of Ebeko down to the Pacific coast of Paramushir, where the town of Severo-Kurilsk is located, which makes it very promising for the geothermal energy exploitation. However, more detailed characteristics of this layer should be identified using alternative geophysical surveys, such as magnetotelluric sounding.

Author statement

NB and YB have developed algorithms for data processing and

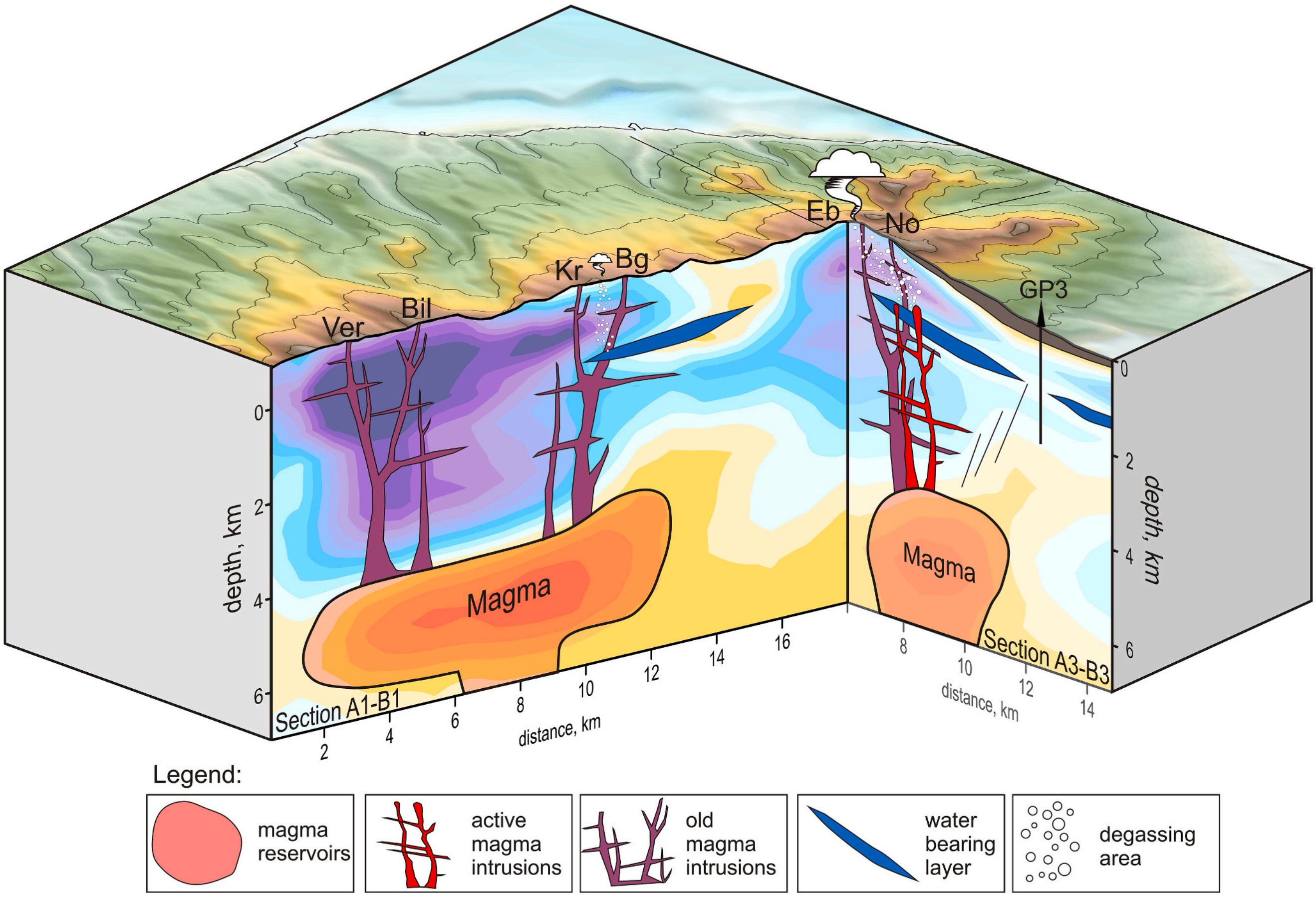

Fig. 11. Interpretation of the resulting velocity anomalies in Sections A1-B1 and A3-B3. Abbreviations of volcanoes: Ver - Vernadsky; Bil - Bilibin; Kr- Krasheninnikov; Bg - Bogdanivich; Eb - Ebeko; No - Neozhidanny;

performed calculations. IK adapted his surface-wave tomography algorithm and performed calculations. AJ and IA were responsible for the field data. SA performed data preprocessing. SZS was responsible for the geological review and interpretation. All the authors participated in discussion of the results and contributed in writing the text and preparing figures.

Declaration of Competing Interest

The authors declare that they have no known competing financial interests or personal relationships that could have appeared to influence the work reported in this paper.

Data availability

All the data used for tomography are available on Zenodo together with the code to reproduce the results

Acknowledgments

The signal processing from the raw data to the dispersion curves was carried out by NB and YB within the state assignment according to the research project FSUS-2022-0019. The work on interpretation of results was supported by the state assignment according to the research project FWZZ-2022-0017. The contribution of IK, who performed the ambient noise tomography, was supported by the Russian Science Foundation Grant #20-17-00075P.

The authors extend their gratitudes to Tatyana and Leonid Kotenko (IVS FEB RAS, Petropavlovsk Kamchatsky, Russia) and also to Mark Kotenko for their full assistance in organization of seismic network deployment and fieldwork on Vernadsky Ridge.

All the results of surface wave tomography presented in this study can be reproduced with the use of the SURF_TOMO code and data openly available on Zenodo at: Ivan Koulakov, Nadezhda Belovezhets, & Yaroslav Berezhnev. (2023). Data and program codes to reproduce the results of surface-wave tomography for the Paramushir Island (Kuril Arc) [Data set]. Zenodo. https://doi.org/10.5281/zenodo.8112137

References

Atlas of Geology and Geophysics in the Kuril-Kamchatka Arc System, 1987. VSEGEI, Leningrad, 36p.

Avdeiko, G.P., Savelyev, D.P., Palueva, A.A., Popruzhenko, S.V., 2007. Evolution of the Kurile–Kamchatkan volcanic arcs and dynamics of the Kamchatka–Aleutian junction. In: Eichelberger, J., Gordeev, E., Izbekov, P., Lees, J. (Eds.), Volcanism and Subduction: The Kamchatka Region. AGU Geophys. Monograph 172, Washington, DC, pp. 41–60.

Bai, T., Nayak, A., Thurber, C., Zeng, X., Haney, M., 2021. Ambient noise tomography of the Katmai volcanic area, Alaska. J. Volcanol. Geotherm. Res. 419, 107373.

Belousov, V.I., Rychagov, S.N., Sugrobov, V.M., 2002. North-Paramushir hydrothermal-magmatic system: geological structure, conceptual model, geothermal resources. Volcanol. Seismol. 1, 34–50.

Belousov, A., Belousova, M., Auer, A., Walter, T., Kotenko, T., 2021. Mechanism of the historical and the ongoing Vulcanian eruptions of Ebeko volcano, Northern Kuriles. Bull. Volcanol. 83, 4. https://doi.org/10.1007/s00445-020-01426-z.

Belovezhets, N.N., Berezhnev, Y.M., Jakovlev, A.V., Abramenkov, S.S., Abkadyrov, I.F., 2022. Detection of clock errors in seismic records and estimation of time shifts for a seismic network. Russian J. Geophys. Technolog. 1, 134–142 (In Russian). 10.18303/2619-1563-2022-1-134.

Bensen, G., Ritzwoller, M., Barmin, M., Levshin, A., Lin, F., Moschetti, M., Shapiro, N., Yang, Y., 2007. Processing seismic ambient noise data to obtain reliable broad-band surface wave dispersion measurements. Geophys. J. Int. 169, 1239–1260.

Bergal-Kuvikas, O., Buslov, M., Bushenkova, N.A., Dolgaya, A.A., 2023. Transition from continental margin to ocean arc of the Kuril Islands: features of volcanism, deformations of the crust and geophysical parameters of the slab. Russ. Geol. Geophys. 64 (10), 1227–1240. https://doi.org/10.15372/GiG2023136.

Bogdanov, A.I., 1981. Report on the results of geophysical surveys of geothermal water on the Ebeko area (Paramushir Island) in 1980. In: Founds of the Sakhalin Geophysical Expedition. Yuzhno-Sakhalinsk.

Bortnikova, S.B., Bessonova, E.P., Trofimova, L.B., Kotenko, T.A., Nikolayeva, N.V., 2006. Hydrogeochemistry of thermal springs of Ebeko volcano (Paramushir Island). Vulcanologia I Seismologia 1, 39–51 (in Russian).

Christensen, N.I., 1996. Poisson's ratio and crustal seismology. J. Geophys. Res. Solid Earth 101, 3139–3156.

D'Auria, L., Koulakov, I., Prudencio, J., Cabrera-Pérez, I., Barrancos, J., García-Hernández, R., Martínez van Dorth, D., Padilla, G.D., Przeor, M., Ortega, V., Hernández, P., Pérez, N.M., 2022. Voluminous storage and rapid magma ascent beneath La Palma revealed by seismic tomography. Sci. Rep. 12, 17654. https://doi.org/10.1038/s41598-022-21818-9.

Díaz-Moreno, A., Barberi, G., Cocina, O., Koulakov, I., Scarfì, L., Zuccarello, L., Prudencio, J., García-Yeguas, A., Álvarez, I., García, L., Ibáñez, J.M., 2017. New insights on Mt. Etna's crust and relationship with the regional tectonic framework from joint active and passive P-wave seismic tomography. Surv. Geophys. https://doi.org/10.1007/s10712-017-9425-3.

Duffield, W.A., Sass, J.H., 2003. Geothermal energy: Clean power from the earth's heat (Vol. 1249). US Geolg. Surv. 36–p.

Dziewonski, A.M., Bloch, S., Landisman, M., 1969. A technique for the analysis of transient seismic signals. Bull. Seismol. Soc. Am. 59, 427–444.

Fedorchenko, V.I., Abdurakhmanov, A.I., Rodionova, R.I., 1989. Volcanism of the Kurile Island Arc: Geology and Petrogenesis. Nauka Moscow, 237 pp.(in Russian).

Girina, O., Manevich, A., Melnikov, D., Nuzhdaev, A., Petrova, E., 2019. The 2016 Eruptions in Kamchatka and on the North Kuril Islands: the Hazard to Aviation. J. Volcanol. Seismol. 13, 157–171.

Gorbatov, A., Fukao, Y., Widiyantoro, S., Gordeev, E., 2001. Seismic evidence for a mantle plume oceanwards of the Kamchatka–Aleutian trench junction. Geophys. J. Int. 146 (2), 282–288.

Gorshkov, G.S., 1970. Volcanism of the Upper Mantle: Investigations in the Kuril Island Arc. Plenum Press, NY (385 pp.).

Gudmundsson, A., 2000. Active fault zones and groundwater flow. Geophysical Research Letters 27 (18), 2993–2996.

Hable, S., Sigloch, K., Barruol, G., Stahler, S.C., Hadziioannou, C., 2018. Clock errors in land and ocean bottom seismograms: high-accuracy estimates from multiple-component noise cross-correlations. Geophys. J. Int. 214, 2014–2034.

Heap, M.J., Baumann, T., Gilg, H.A., Kolzenburg, S., Ryan, A.G., Villeneuve, M., Clynne, M.A., 2021. Hydrothermal alteration can result in pore pressurization and volcano instability. Geology 49 (11), 1348–1352.

Herrmann, R.B., 1987. Computer Programs in Seismology. Saint Louis Univ, St. Louis, Mo. http://www.eas.slu.edu/People/RBHerrmann/CPS330.html.

Jaxybulatov, K., Shapiro, N.M., Koulakov, I., Mordret, A., Landès, M., Sens-Schönfelder, C., 2014. A large magmatic sill complex beneath the Toba caldera. Science 6209 (346), 617–619. https://doi.org/10.1126/science.1258582.

Jiang, G., Zhao, D., Zhang, G., 2009. Seismic tomography of the Pacific slab edge under Kamchatka. Tectonophysics 465 (1), 190–203.

Kalacheva, E.G., Kotenko, T.A., 2013. Chemical composition and the origin of the Upper Yurievskie thermal springs (Paramushir, Kuril Islands). Vestnik KRAUNTS 2 (22), 55–68 (in Russian).

Kalacheva, E.G., Voloshina, E.V., 2022. Geochemical characteristics of thermal sources in the summit part of the Ebeko Volcano (Paramushir Island, Kuril Arc), Vestnik KRAUNC. Earth Sci. 2, 6–19.

Kalacheva, E., Taran, Y., Kotenko, T., Hattori, K., Kotenko, L., Solis-Pichardo, G., 2016. Volcano–hydrothermal system of Ebeko volcano, Paramushir, Kuril Islands: Geochemistry and solute fluxes of magmatic chlorine and sulfur. J. Volcanol. Geotherm. Res. 310, 118–131. https://doi.org/10.1016/j.jvolgeores.2015.11.006.

Khubaeva, O.R., Bergal-Kouvikas, O.V., Sidorov, M.D., 2022. The problem of the formation and nutrition of the Upper Yuryevsky thermal springs (Paramushir Island, Kuril Islands). Volcanol. Seismol. 3, 43–49.

Kiryukhin, A.V., 2000. Conducting Scientific Research on the Geothermal Systems of Paramushir Island in Connection with the Identification of Shallow Geothermal Reservoirs for the Purpose of Geothermal Water Supply. Geo-T Geothermal Scientific Foundation, Branch of INSTITUTE GIDROPROEKT OJSC, TsSGNEO, Moscow.

Kotenko, T.A., Kotenko, L.V., 2006. Hydrothermal manifestations and heat flow of Ebeko and Krasheninnikov volcanoes (Paramushir Island, Kuril Islands). Vestnik KRAUNC. Earth Sci. 7 (1), 129–137.

Kotenko, T.A., Kotenko, L.V., Shapar, V.N., 2007. Activation of Ebeko volcano in 2005-2006 (the Paramushir Island, North Kuril Islands). Volcanol. Seismol. 5, 3–13.

Kotenko, T.A., Smirnov, S.Z., Timina, T.Y., 2023. Activity of Ebeko volcano in 2022: Mechanism and products of the eruption. Volcanol. Seismol. 4, 3–22.

Koulakov, I.Yu., Dobretsov, N.L., Bushenkova, N.A., Yakovlev, A.V., 2011. Slab shape in subduction zones beneath the Kurile–Kamchatka and Aleutian arcs based on regional tomography results. Russ. Geol. Geophys. 52, 650–667.

Koulakov, I., Maksotova, G., Jaxybulatov, K., Kasatkina, E., Shapiro, N., Luehr, B., Khrepy, S., Al-Arifi, N., 2016. Structure of magma reservoirs beneath Merapi and surrounding volcanic centers of Central Java modeled from ambient noise tomography. Geochem. Geophys. Geosyst. 17 (10), 4195–4211. https://doi.org/10.1002/2016GC006442.

Koulakov, I., Shapiro, N., Sens-Shoenefelder, C., Gordeev, E.I., Jakovlev, A.V., Abkadyrov, I., Chebrov, D., Bushenkova, N., Droznina, S., Senyukov, S., Novgorodova, A., Stupina, T., 2020. Mantle sources of magmatic activity in the Northern group of volcanoes in Kamchatka inferred from earthquake tomography. J. Geophys. Res. Solid Earth. https://doi.org/10.1029/2020JB020097 e2020JB020097.

Koulakov, I., D'Auria, L., Prudencio, J., Cabrera-Pérez, I., Pérez, N.M., Ibáñez, J.M., 2023. Local earthquake seismic tomography reveals the link between crustal structure and volcanism in Tenerife (Canary Islands). J. Geophys. Res. Solid Earth 128. https://doi.org/10.1029/2022JB025798 e2022JB025798.

Laverov, N.P., Dobretsov, N.L., Bondur, V.G., Karamurzov, B.S., Kovalenko, V.I., Melekestsev, I.V., Nechaev, Y.V., Ponomareva, V.V., Rogozhin, E.A., Sobisevich, A. L., Sobisevich, L.E., Fedotov, S.A., Khrenov, A.P., Yarmolyuk, V.V., 2005. Modern and Holocene Volcanism in Russia [in Russian]. Nauka, Moscow.

Levshin, A.L., Yanovskaya, T.B., Lander, A.V., Bukchin, B.G., Barmin, M.P., Ratnikova, L. I., Its, E.N., 1989. Seismic Surface Waves in a Laterally Inhomogeneous Earth. Keilis-Borok V.I. D.: Springer. P, p. 304.

Markhanov, V.A., Potapyev, S.V., 1981. Strukturnoye rayonirovanie Kamchatskoy tektonicheskoy oblasti [Structure zoning of Kamchatka tectonic area]. Nauka, Moscow, 88p. In Russian.

Masterlark, T., Haney, M., Dickinson, H., Fournier, T., Searcy, C., 2010. Rheologic and structural controls on the deformation of Okmok volcano, Alaska: FEMs, InSAR, and ambient noise tomography. J. Geophys. Res. Solid Earth 115 (B2).

McIntosh, J.C., Ferguson, G., 2021. Deep meteoric water circulation in Earth's crust. Geophys. Res. Lett. 48 (5) e2020GL090461.

Melekestsev, I.V., Dvigalo, V.N., Kir'yanov, V., Kurbatov, A.V., Nesmachnyy, I.A., 1993. The Ebeko Volcano (the Kuril Islands): history of eruptive activity and future volcanic hazard. Part 1. Volcanol. Seismol. 3, 69–81 (In Russ.).

Melekestsev, I.V., Dvigalo, V.N., Kirianov, V.Yu., Kurbatov, A.V., Nesmachnyi, I.A., 1994. Ebeko volcano, Kuril Islands: eruptive history and potential volcanic hazards. Part I. Volcanol. Seismol. 15 (3), 339–354.

Menyailov, I.A., Nikitina, L.P., Shapar, V.N., 1985. Results of geochemical monitoring of the activity of Ebeko volcano (Kuril Islands) used for the eruption prediction. J. Geodyn. 3, 259–274.

Mordret, A., Rivet, D., Landès, M., Shapiro, N.M., 2015. Three-dimensional shear velocity anisotropic model of Piton de la Fournaise Volcano (La Réunion Island) from ambient seismic noise. J. Geophys. Res. Solid Earth 120 (1), 406–427.

Moreau, L., Stehly, L., Boué, P., Lu, Y., Larose, E., Campillo, M., 2017. Improving ambient noise correlation functions with an SVD-based Wiener filter. Geophys. J. Int. 211, 418–426.

Nolet, G., 1987. Seismic wave propagation and seismic tomography. In: Seismic Tomography. Springer, Reidel, Dordrecht, pp. 1–23. https://doi.org/10.1007/978-94-009-3899-1_1.

Obermann, A., Lupi, M., Mordret, A., Jakobsdóttir, S.S., Miller, S.A., 2016. 3D-ambient noise Rayleigh wave tomography of Snæfellsjökull volcano, Iceland. J. Volcanol. Geotherm. Res. 317, 42–52.

Paige, C.C., Saunders, M.A., 1982. LSQR: an algorithm for sparse linear equations and sparse least squares. ACM Trans. Math. Softw. 8 (1), 43–71. https://doi.org/10.1145/355984.355989.

Rychagov, S.N., Belousov, V.I., Glavatskikh, G.F., Ladygin, V.M., Sefafimova, E.K., 2002. The North Paramushir magmatic–hydrothermal system: the deep geologic section and a model of the present day mineralization and metallization in the interior of the system. Vulcanol. Seismol. 4, 3–21 (in Russian).

Rychagov, S.N., Belousov, V.I., Kotenko, T.A., Kotenko, L.V., 2010. Gas-hydrothermal system of the Ebeko Volcano (Paramushir Island)—Zone of ascending fluid flow in the structure of the North-Kuril geothermal deposit. In: Proceedings of the World Geothermal Congress, Bali, Indonesia, pp. 25–29.

Sens-Schönfelder, C., 2008. Synchronizing seismic networks with ambient noise. Geophys. J. Int. 174 (3), 966–970.

Shmeleva, Z.I., 1993. Preparation of a geophysical basis for prospecting within the eastern part of the North Paramushir geothermal system (On-land geophysical work). In: In 1991–1993, Yelizovo. Elizovskaya Geophysical Expedition. GGP "Kamchatgeologiya".

Shustova, O.S., 1992. Aerogeophysical surveys of Sakhalin and Kuril Islands. Khabarovsk. Geophysical expedition PGO "Dalgeofizika".

State Geological Map 1:200000, 2001. Kurile Series. Sheets M-56-XII, XVII, XVIII, XXIV, M-57-VII, XIII (Paramushir Isl), M-56-XXIII, XXIX (Onekotan Isl), M-56-XXVIII, XXIX, XXXIV, XXXV (Shiashkotan Isl), M-56-XXXIII, XXXIV, L-56-III, IV (Matua Isl), L-56-II, III, VII, VIII, IX (Simushir Isl). VSEGEI. Map with Explanatory Notes 123p.

Taylor, G., Hillers, G., 2020. Estimating temporal changes in seismic velocity using a Markov chain Monte Carlo approach. Geophys. J. Int. 220 (3), 1791–1803.

Walter, T., Belousov, A., Belousova, M., Kotenko, T., Auer, A., 2020. The 2019 Eruption Dynamics and Morphology at Ebeko Volcano Monitored by Unoccupied Aircraft Systems (UAS) and Field Stations, Remote Sensing in Geology, Geomorphology and Hydrology, 12, p. 1961.

Wohletz, K., Heiken, G., 1992. Volcanology and Geothermal Energy, vol. 432. University of California Press, Berkeley.

Zlobin, T.K., 1987. The Structure of the earth's Crust and Upper Mantle of the Kuril Island Arc (According to Seismic Data). DVNC, Vladivostok.

Zollo, A., Gasparini, P., Virieux, J., Biella, G., Boschi, E., Capuano, P., de Franco, R., Dell'Aversana, P., de Matteis, R., De Natale, G., Iannaccone, G., Guerra, I., Le Meur, H., Mirabile, L., 1998. An image of Mt. Vesuvius obtained by 2D seismic tomography. J. Volcanol. Geotherm. Res. 82 (1–4), 161–173.